Dalton Transactions

PAPER

View Article Online
View Journal | View Issue



Cite this: *Dalton Trans.*, 2019, **48**, 9376

# Lithium ion dynamics in $LiZr_2(PO_4)_3$ and $Li_{1.4}Ca_{0.2}Zr_{1.8}(PO_4)_3$†

Isabel Hanghofer,*[a] Bernhard Gadermaier,[a] Alexandra Wilkening,[a] Daniel Rettenwander[a] and H. Martin R. Wilkening*[a,b]

High ionic conductivity, electrochemical stability and small interfacial resistances against Li metal anodes are the main requirements to be fulfilled in powerful, next-generation all-solid-state batteries. Understanding ion transport in materials with sufficiently high chemical and electrochemical stability, such as rhombohedral $LiZr_2(PO_4)_3$, is important to further improve their properties with respect to translational Li ion dynamics. Here, we used broadband impedance spectroscopy to analyze the electrical responses of $LiZr_2(PO_4)_3$ and Ca-stabilized $Li_{1.4}Ca_{0.2}Zr_{1.8}(PO_4)_3$ that were prepared following a solid-state synthesis route. We investigated the influence of the starting materials, either $ZrO_2$ and $Zr(CH_3COO)_4$, on the final properties of the products and studied Li ion dynamics in the crystalline grains and across grain boundary (g.b.) regions. The $Ca^{2+}$ content has only little effect on bulk properties ($4.2 \times 10^{-5}$ S cm$^{-1}$ at 298 K, 0.41 eV), but, fortunately, the g.b. resistance decreased by 2 orders of magnitude. Whereas, $^7$Li spin-alignment echo nuclear magnetic resonance (NMR) confirmed long-range ion transport as seen by conductivity spectroscopy, $^7$Li NMR spin–lattice relaxation revealed much smaller activation energies (0.18 eV) and points to rapid localized Li jump processes. The diffusion-induced rate peak, appearing at $T$ = 282 K, shows $Li^+$ exchange processes with rates of *ca.* $10^9$ s$^{-1}$ corresponding, formally, to ionic conductivities in the order of $10^{-3}$ S cm$^{-1}$ to $10^{-2}$ S cm$^{-1}$.

Received 29th April 2019,
Accepted 2nd June 2019

DOI: 10.1039/c9dt01786k

rsc.li/dalton



## 1. Introduction

In the years to come, all-solid-state Li or Na batteries[1] are expected to replace conventional systems[2] that still rely on flammable aprotic electrolytes. Ceramic cells may take advantage of highly flexible design possibilities if batteries with dimensions in the mm range are considered.[3,4] Moreover, ceramic batteries are going to withstand higher temperatures than their analogous cells with liquid components.[5]

For their realization, ceramic electrolytes with sufficiently high ionic conductivities are, however, needed.[5–9] The overall performance of NaSICON-type (Na SuperIonic CONductor) conductors[10,11] has attracted renewed interest to study the influence of synthesis conditions and dopants on morphology and ion dynamics. Earlier reports have shown that $LiM_2(PO_4)_3$ (M: Ge, Ti, Sn, Hf, Zr) exhibits good chemical stabilities under ambient conditions. This property comes along with a wide electrochemical stability window.[12,13] $LiTi_2(PO_4)_3$ is known as a very good Li-ion conductor but it suffers from the fact that Ti(IV) can easily be reduced to Ti(III) when in contact with metallic Li.[14]

In contrast to $LiTi_2(PO_4)_3$-based ceramics, including those in which $Ti^{4+}$ is partly replaced by $Al^{3+}$, $LiZr_2(PO_4)_3$ (LZP) shows a much better stability against Li anodes. If in contact with a Li metallic anode LZP forms stable decomposing products, such as $Li_3P$ and layer-structured $Li_8ZrO_6$, that are able to conduct Li ions when present as thin layers. Importantly, this interphase also reveals sufficiently good wetting properties with respect to both Li metal and the electrolyte.[15] LZP crystallizes with different structures, ionic conductivities sensitively depend on both the overall morphology and the defect chemistry involved. The ionic conductivity can be improved by incorporating different metals such as $Y^{3+}$, $Sc^{3+}$, $Al^{3+}$, $La^{3+}$ or $Ca^{2+}$; this strategy is usually accompanied by a stabilization of the rhombohedral structure.[13,16–22] LZP is typically prepared at calcination temperatures of *ca.* 1173 K, the phase appearing under these conditions is denoted as the α-phase of LZP, which is subdivided in a orthorhombic form (α) and a monoclinic one (α′). At higher sintering temperatures, that is, approximately at 1423 K, the highly conductive rhombohedral structure α-$LiZr_2(PO_4)_3$ crystallizing with $R\bar{3}c$ symmetry is

[a]*Institute for Chemistry and Technology of Materials, Christian Doppler Laboratory for Lithium Batteries, Graz University of Technology (NAWI Graz), Stremayrgasse 9, A-8010 Graz, Austria. E-mail: isabel.hanghofer@tugraz.at*
[b]*ALISTORE – European Research Institute, CNRS FR3104, Hub de l'Energie, Rue Baudelocque, 80039 Amiens, France. E-mail: wilkening@tugraz.at*

†Electronic supplementary information (ESI) available: Further X-ray powder patterns, results from structure solution and Nyquist plots. See DOI: 10.1039/c9dt01786k

formed. α′-$LiZr_2(PO_4)_3$, obtained at lower temperatures, is usually a mixture of monoclinic LZP and triclinic LZP; its ionic conductivity is reported to be in the order of $10^{-8}$ S $cm^{-1}$ whereas α-$LiZr_2(PO_4)_3$ shows values around $10^{-5}$ S $cm^{-1}$.[15,22–25]

In this work, the structure variation of different educts on the product formed is discussed. We analysed Li ion dynamics in $LiZr_2(PO_4)_3$ and $Li_{1+2x}Ca_xZr_{2-x}(PO_4)_3$ (LCZP) by both broadband impedance spectroscopy[26,27] and $^7$Li nuclear magnetic resonance (NMR) spectroscopy, *i.e.*, by recording diffusion-induced spin–lattice relaxation rates.[28–30] The latter are sensitive to both short-range and long-range ion transport through the crystal lattice of LZP. As we deal with powder samples with crystallite diameters in the μm range, NMR rates measured in the laboratory frame of reference are solely sensitive to bulk ion dynamics.

## 2. Experimental

### 2.1. Sample preparation

$LiZr_2(PO_4)_3$ (LZP) was prepared *via* a classic solid-state reaction by mixing stoichiometric amounts of $Li_2CO_3$ (Sigma Aldrich ≥99%), $(NH_4)_2HPO_4$ (Sigma Aldrich ≥99.9%) with either $ZrO_2$ (Sigma Aldrich ≥99%) or $Zr(CH_3COO)_4$ (= $Zr(ac)_4$). The starting compounds were mechanically milled for 2 hours by using a high-energy planetary ball mill (Fritsch Pulverisette 7 Premium line) at a rotation speed of 400 rpm. We used $ZrO_2$ beakers (45 mL), which were filled with 180 balls made of $ZrO_2$ (5 mm in diameter). The subsequent calcination process was carried out in $Al_2O_3$ crucibles at 900 °C (heating rate 10 °C $min^{-1}$) for 10 hours, where the decomposition of the hydrogen phosphate starts and initiates the reaction with $Li_2CO_3$. The resulting white powder was milled again for 2 hours at 400 rpm to guarantee a good contact between the particles. Finally, the mixture was pressed with 0.4 tons into pellets with a diameter of 5 mm. The pellets were filled into $Al_2O_3$ crucibles and sintered at 1150 °C (heating rate 10 °C $min^{-1}$) for 20 hours. To incorporate $Ca^{2+}$ into LZP we used $CaCO_3$ (Alfa Aesar, >99%). An excess of 10 wt% $Li_2CO_3$ should compensate the loss of lithium during the high temperature heating process leading to $Li_{1.4}Ca_{0.2}Zr_{1.8}(PO_4)_3$ (LCZP). For the synthesis of LZP (and LCZP) using $Zr(CH_3COO)_4$ we needed to prepare the acetate as follows.[31] 20 mmol Zirconium oxochloride (Sigma-Aldrich 99.99%) was dissolved under reflux in 100 mL of a mixture of MeCOOH (Sigma-Aldrich ≥99.5%) and $Me(COO)_2O$ (Sigma Aldrich ≥99%) (1 : 9). After the mixture was allowed to cool to room temperature, a white crystalline deposit appeared. Finally, it was filtered and dried at 60 °C under vacuum.

### 2.2. X-ray powder diffraction

The sample obtained after the calcination process and the finally sintered product were characterized by X-ray powder diffraction (XRPD). We used a Bruker D8 Advance diffractometer operating with Bragg Brentano geometry and Cu $K_\alpha$ radiation. Diffractograms were recorded in air atmosphere and at room temperature covering a $2\theta$ range from 20° to 100° with a step size of 0.02° (2 s per step). Rietveld analysis (X-PertHighScorePlus (PANanalytical)) was used to refine the diffraction data.

### 2.3. Impedance spectroscopy

For the impedance measurements the sintered samples were equipped with gold electrodes by a sputtering process. Gold electrodes with a layer thickness of 100 nm were applied on both sides with a sputter coater (LEICA EM SCD 050) to ensure a good electrical contact. To avoid any influence of moisture, the samples were dried at 60 °C under vacuum prior to the impedance measurements.

Impedance spectra were recorded with a Novocontrol Concept 80 broadband dielectric spectrometer equipped with a BDS 1200 cell combined with an active ZGS cell (Novocontrol). We measured complex impedances over a frequency range of ten decades (10 mHz to 10 MHz). The temperature in the sample holder was varied from 173 K to 473 K in steps of 20 K; the temperature program was automatically controlled by a QUATRO cryosystem (Novocontrol). During the measurements a dry nitrogen atmosphere was build up around the sample in the cryostat to avoid any contamination with water and/or oxygen.

### 2.4. Nuclear magnetic resonance measurements

For the time-domain NMR measurements, the powder samples $LiZr_2(PO_4)_3$ and $Li_{1.4}Ca_{0.2}Zr_{1.8}(PO_4)_3$ were sealed in Duran glass tubes (*ca.* 4 cm in length and 3 mm in diameter). During the sealing procedure they were kept under dynamic vacuum to safely protect them from any contact with humid air. We used $^7$Li NMR line shape measurements, spin lattice relaxation (SLR) experiments as well as $^7$Li spin alignment echo (SAE) NMR to collect information about Li activation energies and jump rates. Longitudinal NMR SLR rates ($1/T_1$) as well as spin-lock rates ($1/T_{1\rho}$) were measured with a Bruker Avance III spectrometer that is connected to a shimmed cryomagnet with a nominal magnetic field of 7 Tesla. This field corresponds to a $^7$Li Larmor frequency of $\omega_0/2\pi$ = 116 MHz. For the measurements at temperatures ranging from 173 K to 583 K a ceramic temperature probe (Bruker Biospin) was used. Depending on temperature and at a power level of 180 W the π/2 pulse length ranged from 2.2 μs to 2.4 μs.

$^7$Li NMR SLR rates ($1/T_1 = R_1$) in the laboratory frame were acquired with the well-known saturation recovery pulse sequence. This sequence uses a comb of closely spaced π/2 pulses to destroy any longitudinal magnetization $M_z$. The subsequent recovery of $M_z$ was detected as a function of waiting time $t_d$ with a π/2 reading pulse: 10 × π/2 − $t_d$ − π/2 − acquisition.[32,33] To construct the magnetization transients $M_z(t_d)$, we plotted the area under the free induction decays *vs.* $t_d$. The transients $M_z(t_d)$ were parameterized with stretched exponentials, $M_z(t_d) \propto 1 - \exp(-(t/T_1)^\gamma)$, to extract the rates $R_1$. Additionally, rotating frame $^7$Li NMR SLRρ rates $1/T_{1\rho}$ (= $R_{1\rho}$) were measured by means of the spin lock technique: π/2-$p_{lock}$ − acquisition.[32] Here, we used a locking frequency $\omega_1/2\pi$ of 20 kHz. The duration of the spin-lock pulse $t_{lock}$ was varied

from 10 μs to 460 ms. To ensure full longitudinal relaxation between each scan the recycle delay was set to 5 × $T_1$. The $R_{1\rho}$ rates were obtained by analyzing the resulting transients $M_\rho(t_{lock})$ with stretched exponentials with the form $M_\rho(t_{lock}) \propto \exp(-(t_{lock}/T_{1\rho})^\kappa)$. The stretching exponent $\gamma$ varied from 1 to 0.8, the exponent $\kappa$ ranges from 1 to 0.6.

Finally, mixing time ($t_m$) dependent $^7$Li SAE NMR decay curves were recorded with the help of the Jeener–Broekaert[34,35] three-pulse sequence: (90°)X-$t_p$–(45°)Y-$t_m$–45°-acq. We used a constant preparation time $t_p$ of 25 μs to acquire two-time sinus–sinus single-spin correlation functions. The mixing time was varied from 30 μs up to several seconds. A suitable phase cycle[34,36] was employed to suppress unwanted coherences and to eliminate, as best as possible, dipolar contributions affecting the echo that appears after the reading pulse.[36] Fourier transformation of the spin alignment echoes, starting from the top of the signal, yields $^7$Li SAE NMR spectra useful to highlight quadrupole intensities due to the interaction of the quadrupole moment of the $^7$Li spin (spin-quantum number $I$ = 3/2) and a non-vanishing electric field gradient.

## 3. Results and characterization

### 3.1. Characterization *via* X-ray powder diffraction

The purity of the crystalline samples synthesized was examined by XRPD. As mentioned above, diffraction patterns were collected at room temperature and under air atmosphere. The first XRPD pattern was recorded directly after the calcination process, *i.e.*, after removal of $CO_2$, $NH_3$ and $H_2O$ at 900 °C, the pattern is depicted in Fig. S1.† After this calcination step (10 hours), we see that $LiZr_2(PO_4)_3$ crystallizes with monoclinic structure (space group $P12_1/c1$, see Fig. S1 (ESI)†). Sintering the samples yields a crystalline material that is in agreement with the rhombohedral NaSICON structure[37] (space group $R\bar{3}c$, Fig. 1);[19] the corresponding XRPD pattern is shown in Fig. 2. This phase is isostructural with the sibling compound $LiTi_2(PO_4)_3$.[38] The increase in conductivity before and after sintering, *i.e.*, the difference in ionic transport properties of monoclinic and rhombohedral LZP is illustrated in Fig. S1b.†

The $Zr_2(PO_4)_3$ framework of rhombohedral NaSICON-type LZP consists of two $ZrO_6$ octahedra and three $PO_4$ tetrahedra sharing O atoms. The octahedral and tetrahedral units are alternating with the cations to form infinite chains parallel to the ternary axis of the structure. Each $PO_4$ unit shares its

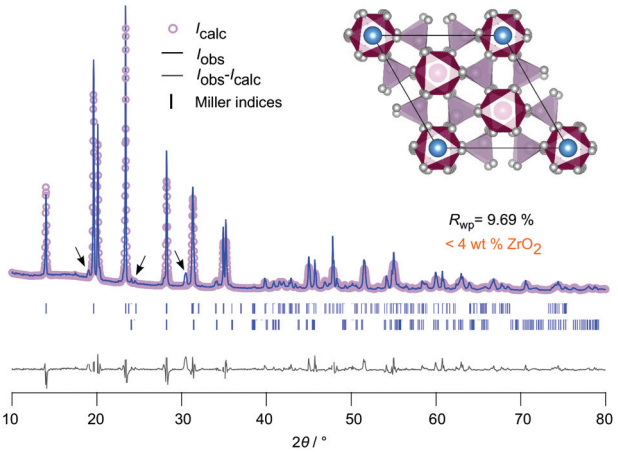


**Fig. 2** Rietveld refinement of LZP using $ZrO_2$ as educt. The sample was sintered at 1150 °C for 20 hours in a closed $Al_2O_3$-crucible. LZP crystallizes with space group $R\bar{3}cH$, see Table S1† for further information. Selected reflections have been indexed with vertical bars. A very small amount (<4 wt%) of $ZrO_2$ was detected. The inset shows the *ab*-plane of the rhombohedral NaSICON structure with the viewing direction along the *c*-axis.

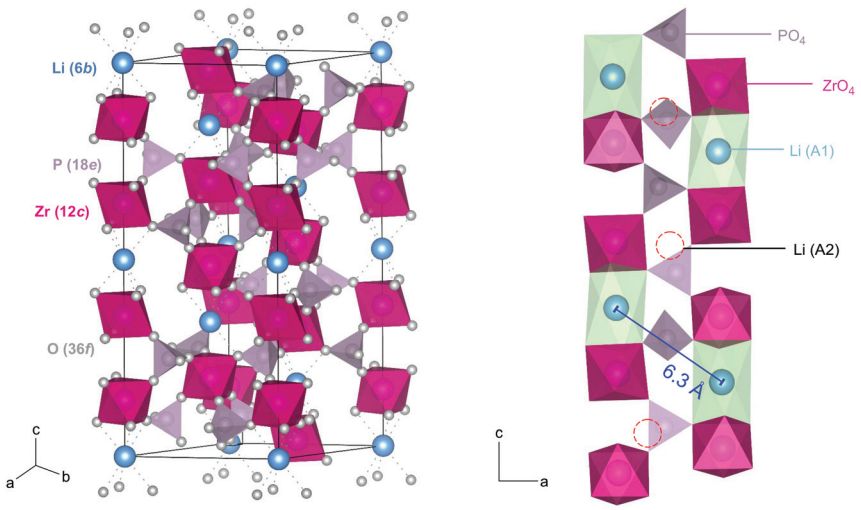


**Fig. 1** Left: Rhombohedral crystal structure of $LiZr_2(PO_4)_3$. The tetrahedra in purple represent $PO_4$-units, octahedra in pink show $ZrO_6$, while the blue spheres denote the $Li^+$ ions. $Li^+$ is octahedrally coordinated by oxygen anions of the $ZrO_6$ octahedra. Right: Section of the rhombohedral crystal structure to show interstitial sites A2; the Li ions may use to jump between the regularly occupied sites A1. The A1–A1 distance is 6.3 Å, which is, presumably, much too large for a direct jump process.

 

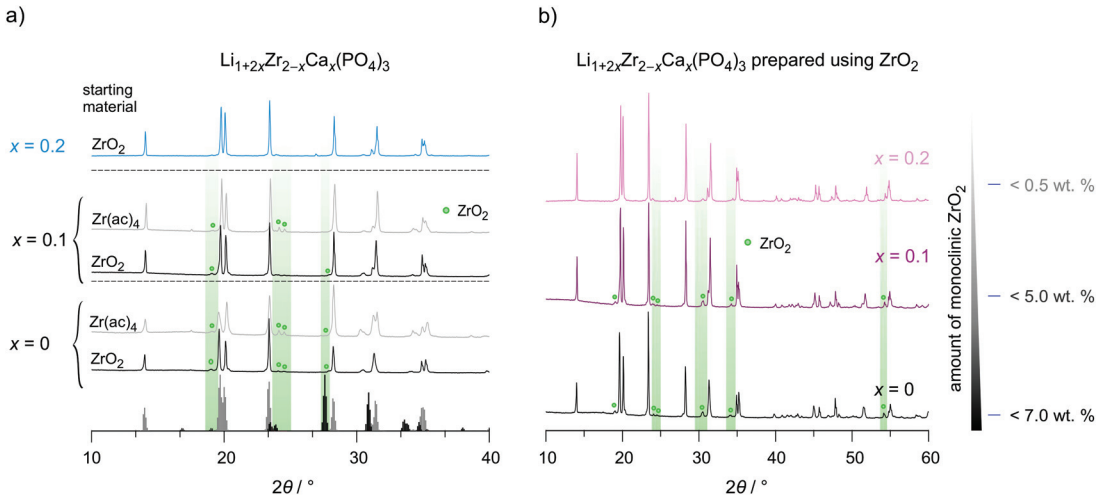


**Fig. 3** (a) X-ray powder diffraction pattern of the crystalline $LiZr_2(PO_4)_3$ and $Li_{1+2x}Zr_{2-x}Ca_x(PO_4)_3$ ($x$ = 0.1 and 0.2). All samples were prepared by a classical solid-state route with either $ZrO_2$ as starting material (black) or $Zr(CH_3COO)_4$ (light grey). The vertical lines (in grey) at the bottom denote the reflections of rhombohedral LZP, those of monoclinic $ZrO_2$ are indicated by green dots. (b) XRPD pattern of $Li_{1+2x}Zr_{2-x}Ca_x(PO_4)_3$ prepared with the help of $ZrO_2$. The diffraction pattern reveal that the amount of the impurity phase $ZrO_2$ decreases with increasing $Ca^{2+}$-content.

oxygen with four $ZrO_6$ octahedra of three $Zr_2(PO_4)_3$ units to form the NaSICON framework. A 3D network of conduction pathways is formed that is used by the ions to diffuse through the crystal. In this case the Li ions (6*b*) are octahedrally coordinated by oxygen ions (36*f*) at the intersection of three conduction channels (A1). The A1 sites are located between pairs of $ZrO_6$ octahedra along the *c*-axis, while the (vacant) interstitial sites (□) A2 can be found between $O_3ZrO_3A1O_3Zr$-□-$O_3ZrO_3A1$. Since the A1–A1 distance in LZP is rather larger, we assume that interstitial sites, such as A2, are involved in $Li^+$ diffusion. Because of the large spatial separation of Li ions in LZP, we expect rather low homonuclear dipole–dipole interactions resulting in narrow $^7$Li NMR lines even in the rigid lattice regime, see below.

In Fig. 2 the result of our Rietveld analysis of the diffraction pattern of $LiZr_2(PO_4)_3$ synthesized by using $ZrO_2$ as educt is shown. Our structure solution indeed points to rhombohedral symmetry characterized by the space group $R\bar{3}cH$ (ICSD, no. 201935), as already found by the study of Petit *et al.*[19] *Via* high-temperature neutron diffraction ($T \geq 423$ K), Catti *et al.* reported on two $Li^+$ positions displaced from the A1 and A2 sites (see Fig. S2†).[24] Here, in addition to the main rhombohedral phase, a minor impurity of $ZrO_2$ (<4 wt%) is seen (see black bars). Rietveld analysis yields the following lattice properties $a$ (= $b$) = 8.824 Å and $c$ = 22.456 Å; $V$ = 1514.24 Å$^3$. By doping this sample with 5 wt% and 10 wt% $Ca^{2+}$ the cell volume decreases (1512.64 Å$^3$ (5 wt% Ca), 1506.22 Å$^3$ (10 wt% Ca)) as expected; for further information we refer to Table S1 in the ESI.†

The preparation route with $Zr(CH_3COO)_4$ as starting material yields almost the same lattice parameters but the amount of non-reacted material is much higher and reaches values as high as 25 wt%. The incorporation of aliovalent $Ca^{2+}$ ions, on the other hand, helps obtaining phase pure LZP with rhombohedral structure, as is illustrated in Fig. 3. The amount of unreacted $ZrO_2$ continuously decreases with increasing Ca-content. This behavior is also found for LCZP prepared with the help of $Zr(ac)_4$. Nonetheless, the amount of $ZrO_2$ remains much higher (>15 wt%) than that in samples prepared from $ZrO_2$ directly. Dots in Fig. 3 denote reflections belonging to $ZrO_2$. Worth noting, here we do not find any additional Bragg reflections that belong to triclinic LZP in all diffractograms. These have been seen in earlier reports.[22,39–41] We recognize that small variations in synthesis conditions, including heat treatment and cooling rates, might sensitively affect the phase purity of the final compounds.

According to XRPD we decided to study, in detail, ion dynamics of the following samples: $LiZr_2(PO_4)_3$ prepared from $ZrO_2$ and $Zr(ac)_4$ as well as $Li_{1+2x}Zr_{2-x}Ca_x(PO_4)_3$ ($x$ = 0.1 and 0.2) prepared with the help of $ZrO_2$. Similar to $LiTi_2(PO_4)_3$ and other NaSICON-type materials α-$LiZr_2(PO_4)_3$ shows low relative densities, here ranging from 78% to 84%.

### 3.2. Impedance spectroscopy

To study how $Li^+$ ion transport is affected by $x$ as well as to investigate whether the starting materials influence the dynamic parameters, we measured complex impedances over a large temperature and frequency range.[26,42] Exemplarily, in Fig. 4a conductivity isotherms of rhombohedral $LiZr_2(PO_4)_3$ are shown. Isotherms are obtained by plotting the real part, $\sigma'$, of the complex conductivity $\sigma$ of $LiZr_2(PO_4)_3$ as a function of frequency $\nu$. They are composed of four regimes. (i) At low frequencies (and sufficiently high temperatures and, thus, high ionic mobility) electrode polarization (EP) appears owing to the piling-up of ions near the surface of the blocking Au electrodes applied. In many cases a stepwise decay of $\sigma'$ is seen (*cf.* the two arrows in Fig. 4a). (ii) The polarization regime passes into so-called conductivity plateaus (P1) governing the iso-

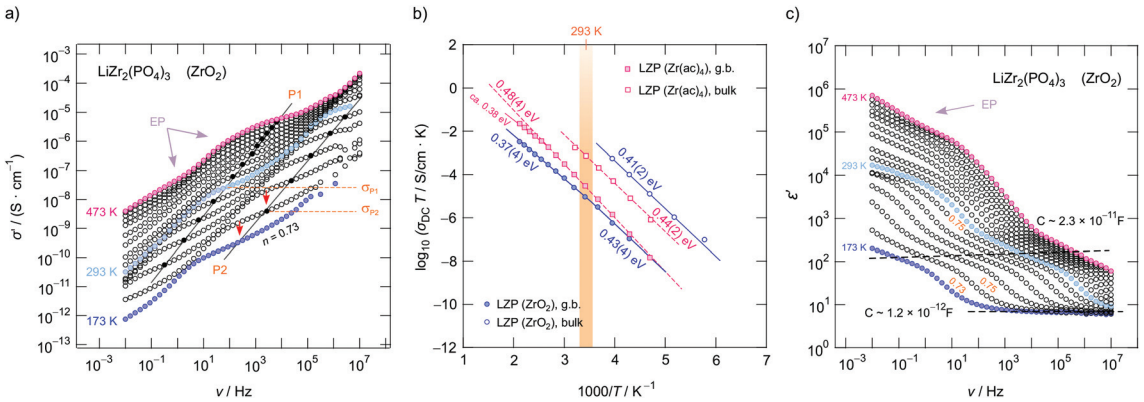


**Fig. 4** (a) Conductivity isotherms of Ca-free LZP (synthesized from $ZrO_2$) recorded at temperatures ranging from 173 K to 473 K; isotherms have been recorded in steps of 20 K. We observed two plateaus P1 and P2 that correspond to the grain boundary (g.b., P1) and bulk response (P2). (b) Arrhenius plot of the DC conductivities associated with P1 and P2. The solid and dashed line show line fits with an Arrhenius law yielding activation energies ranging from 0.39 eV to 0.52 eV. Circles represent LZP synthesized from $ZrO_2$ and rectangles show results of LZP that was synthesized from $Zr(ac)_4$. LZP prepared from $ZrO_2$ shows the highest bulk ion conductivity that is characterized by 0.41 eV. (c) Real part of the complex permittivity as a function of frequency. P1 and P2 seen in (a) produce a two-step increase of $\varepsilon'$ characterized by permittivities and capacities being typical for a bulk electrical response and a response including ion-blocking grain boundaries. The same characteristics are seen for LZP prepared from $Zr(ac)_4$. Both processes can be approximated with a power law of the form $\varepsilon'(\nu) = \varepsilon(\infty) + A_s\nu^{-p}$ with $p \neq f(T) \approx 0.75$, wherein $\varepsilon(\infty)$ represents the permittivity at very high frequencies.

therms at intermediate temperatures and low frequencies. If this plateau is identified with a bulk response, it reflects long-range ion transport and is given by the dc-conductivity $\sigma_{dc}$. By moving to higher frequency a shallow dispersive regime with a weak frequency dependence shows up. It directly merges into another plateau (iii, P2), which finally passes over in the high-frequency dispersive regime (iv) which can roughly be approximated with Jonscher's power law.

In Fig. 4a the inflexion points of the plateaus P1 and P2 are highlighted by filled circles; straight lines connect these circles. The dispersive region belonging to plateau P2 is best seen at 173 K, it can be approximated with Jonscher's power law:[43] $\sigma' = \sigma_{dc} + A_0\nu^n$. Here $A_0$ is the so-called dispersion parameter and $n$ represents the power law exponent, which takes a value of 0.73 at 173 K. To analyse our data in terms of dimensionality effects, we also studied the frequency dependence of the real part of the complex permittivity; the corresponding isotherms ($\varepsilon'$ *vs.* $\nu$) are plotted in Fig. 4c; the plateaus P1 and P2 produce a two-step increase of $\varepsilon'$ when coming from high frequencies. As for $\sigma'$, also $\varepsilon'(\nu)$ can be approximated with exponents around 0.75 for P2, see Fig. 4c. Such Jonscher exponents are expected for 3D ionic conduction.[44]

To determine which capacitances $C$ govern the responses P1 and P2, we used the equation for a parallel-plate capacitor for an estimation $C = \varepsilon_0\varepsilon_r A/d$. Here $\varepsilon_0$ represents the electric field constant ($8.854 \times 10^{-12}$ F m$^{-1}$), $A$ the area and $d$ the thickness of the sample. While the DC plateau (P2) at high frequencies is characterized by $C = 1.2(1) \times 10^{-12}$ F, for the plateau at lower $\nu$ we found $C = 2.3(2) \times 10^{-11}$ F. Therefore, the plateau associated with $C$ in the pF range represents the bulk response, whereas P1 seen at lower frequencies is additionally governed by grain boundary contributions (g.b.) for which capacitances in the order of $10^{-11}$ F are typically expected.[45]

In the Arrhenius plot of Fig. 4b, $\sigma_{DC}T$ of the two plateaus P1 and P2 is plotted *vs.* the inverse temperature $T$. $\sigma_{DC}T$ does not change when several heating and cooling runs were performed. The lines in Fig. 4b refer to fits according to $\sigma_{DC}T(P1,\ P2) \propto \exp(-E_a/(k_BT))$; $k_B$ denotes the Boltzmann's constant and $E_a$ the corresponding activation energy. For $LiZr_2(PO_4)_3$ prepared from $ZrO_2$ we obtain $E_a(P2)$ of 0.41(1) eV (in agreement with ref. 15 (0.40 eV) and ref. 25 (0.39 eV)), whereas for $LiZr_2(PO_4)_3$, when using $Zr(ac)_4$ as starting material, $E_a$ increases to 0.44(1) eV (see Fig. 4b). At room temperature, the ionic conductivities of P2 are $3.6(2) \times 10^{-5}$ S cm$^{-1}$ and $3.4(2) \times 10^{-6}$ S cm$^{-1}$, respectively. For the sake of clarity, in Table 1 all activation energies $E_a$ are listed, the table also includes values referring to $Li_{1+2x}Ca_xZr_{2-x}(PO_4)_3$ ($x = 0.1$, $x = 0.2$) that has been prepared from $ZrO_2$.

Unfortunately, by using Nyquist diagrams (see Fig. S3†), which show complex plane plots of the imaginary part $Z''$ of the complex impedance, $Z$, *vs.* its real part $Z'$, the faster relaxation process, corresponding to P2, cannot be resolved prop-

**Table 1** Comparison of activation energies $E_a$ and prefactors $\sigma_0$ of the Arrhenius lines shown in Fig. 4b. The values refer to Ca-free and Ca-containing $LiZr_2(PO_4)_3$. Values in the brackets represent data determined by blocking grain boundaries (P2). Results for Ca-bearing LZP are also included

| composition | $E_a$/eV | $\log_{10}(\sigma_0$/S cm$^{-1}$ K) | Starting material |
|---|---|---|---|
| $LiZr_2(PO_4)_3$ | 0.44(2) (0.48(4)) | 4.97(1) (3.86(2)) | $Zr(ac)_4$ |
| $LiZr_2(PO_4)_3$ | 0.41(2) (0.37(4)[a]) | 4.91(2) (1.49(7)) | $ZrO_2$ |
| $Li_{1.2}Ca_{0.1}Zr_{1.9}(PO_4)_3$ | 0.43(1) (0.52(9)) | 5.44(4) (4.14(7)) | $ZrO_2$ |
| $Li_{1.4}Ca_{0.2}Zr_{1.8}(PO_4)_3$ | 0.41(2) (0.38(4)) | 5.08(2) (3.49(1)) | $ZrO_2$ |

[a] At lower temperatures the activation energy increases to 0.43(4) eV.

erly. Instead, we used the complex modulus $M''(\nu)$ representation[46] to visualize the two processes, see Fig. 5a and 6 (Fig. 6b includes data for $Li_{1+2x}Ca_xZr_{2-x}(PO_4)_3$ prepared from $ZrO_2$).

At sufficiently low temperatures two relaxation peaks M1 and M2 appear (see the orange arrows in Fig. 5a). These peaks are separated by two orders of magnitude on the frequency scale. This distance on the frequency scale is comparable with the ratio of $\sigma_{DC,P2} : \sigma_{DC,P1}$; thus, they refer, as is seen in Fig. 6 to the plateaus P1 and P2 governing $\sigma'(\nu)$. As expected the two electrical relaxation frequencies mirror the ratio in conductivities. The peak with the larger amplitude (M2) corresponds

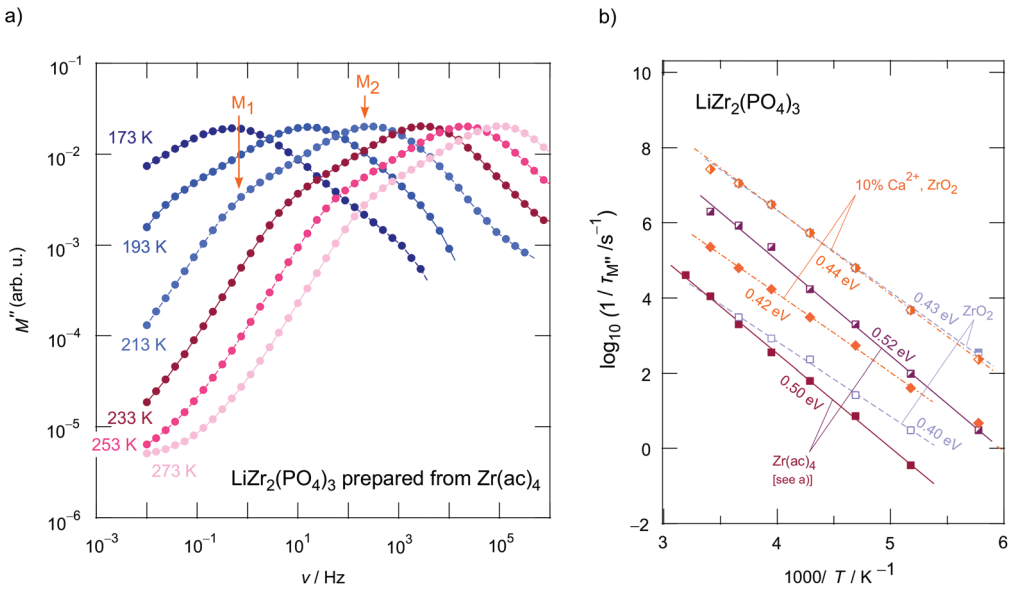


Fig. 5 (a) Frequency dependence of the imaginary part of the electric modulus $M''$, of $LiZr_2(PO_4)_3$ prepared from $Zr(ac)_4$. Spectra were recorded at the temperatures indicated. The lines are to guide the eye. As suggested by $\sigma'(\nu)$, two distinct peaks are visible denoted as M1 and M2. The temperature dependence of the corresponding relaxation rate $\tau_M^{-1}$ is shown in (b). For comparison, the results of $LiZr_2(PO_4)_3$ (prepared from $ZrO_2$) and $Li_{1.4}Zr_{1.8}Ca_{0.2}(PO_4)_3$ (also prepared from $ZrO_2$) are included as well. Error margins are at least ± 0.1 eV.

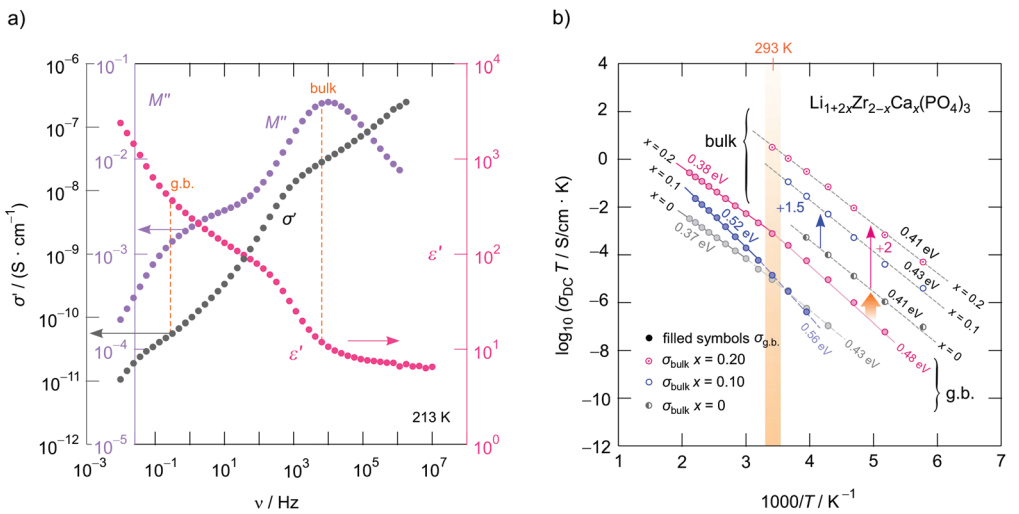


Fig. 6 (a) Frequency dependence of the imaginary part $M''$ of the complex modulus, the real part, $\varepsilon'$, of the permittivity as well as the real part, $\sigma'$, of the complex conductivity of $LiZr_2(PO_4)_3$ (prepared from $ZrO_2$). The isotherm was recorded at 213 K. The maxima in $M''$ clearly refer to the plateaus P1 and P2 seen in $\sigma'(\nu)$. For comparison, the change of $\varepsilon'(\nu)$ is shown, too. (b) Arrhenius plot of the ionic conductivities referring to the plateaus P1 and P2 ($\sigma_{DC}T$ *vs.* $1000/T$) of cation-mixed crystalline $Li_{1+2x}Zr_{2-x}Ca_x(PO_4)_3$. Solid lines and dashed lines represent fits according to an Arrhenius law yielding the activation energies $E_a$ as indicated. While solid lines refer to conductivities influenced by the grain boundary contributions, the dashed lines represent bulk ion dynamics in $Li_{1+2x}Zr_{2-x}Ca_x(PO_4)_3$. For the sake of clarity, the bulk ion conductivities for the samples with $x$ = 0.20 and $x$ = 0.10 have been plotted using an offset of +2 and +1.5 on the logarithmic scale. These conductivities coincide with those of the Ca-free sample. Activation energies with error margins are listed in Table 1.

to P2 in $\sigma'(\nu)$, the one with the smaller amplitude (M1) represents a relaxation process with a longer relaxation time (*cf.* P1), see also Fig. 6. As an estimation, $M''$ is proportional to the inverse capacitance, $M'' \propto 1/C$.[45,47] Thus, we expect peak M2 to be characterized by a larger amplitude (3.4 pF) than M1 (30.1 pF). $C_1/C_2 \approx 10$ is in good agreement with the amplitude ratio seen in Fig. 5a and 6a.

In order to compare activation energies extracted from $\sigma_{DC}$(P1, P2) we determined characteristic electrical relaxation frequencies $1/\tau_M$ using the modulus peaks of Fig. 5a. $1/\tau_M$ refers to frequencies at which the peaks appear. A comparison of activation energies for selected compounds is shown in Fig. 5b; errors are, at least, in the order of ±0.01 eV.

As mentioned in the beginning, $Ca^{2+}$ incorporation increases the ionic conductivity of LZP. Fig. 6b shows the change in $\sigma_{DC}T$(P1, P2) of $Li_{1+2x}Ca_xZr_{2-x}(PO_4)_3$ prepared from $ZrO_2$ for $x$ = 0, $x$ = 0.1 and $x$ = 0.2. Most importantly, while $\sigma_{DC}T$(P2), which refers to bulk ion dynamics, is only slightly affected by $x$ ($E_a$ ranges from 0.41 eV to 0.43 eV, see Fig. 6b and Table 1 that also includes the prefactors), $Ca^{2+}$ incorporation mainly reduces the g.b. resistance. We clearly see that $\sigma_{DC}T$(P1) is by two orders of magnitude larger than that of the sample with $x$ = 0, see Fig. 6b. Most likely, the sintering process benefits from a Ca-rich composition, which helps reducing the blocking nature of surface regions of the $Li_{1+2x}Ca_xZr_{2-x}(PO_4)_3$ crystallites. For $x$ = 0.2 we obtain $\sigma_{DC}$(P2) = $4.2 \times 10^{-5}$ S cm$^{-1}$ at 293 K. This value is only slightly lower than that of Li *et al.*[15] ($3.8 \times 10^{-5}$ S cm$^{-1}$) when samples are compared that have been prepared by conventional sintering. If pellets were fired by spark plasma sintering, bulk values of $1.8 \times 10^{-4}$ S cm$^{-1}$ were reported.[15] It would be interesting to see, in coming studies, whether $Ca^{2+}$, here acting as a sintering aid, segregates in the g.b. regions; such segregation would explain the finding that ion transport in the bulk regions is only little affected by $Ca^{2+}$ incorporation.

Careful inspection of $\sigma_{DC}T$(P1) reveals that, if the samples with $x$ = 0.2 is considered as an example (Fig. 6b), a slight kink is seen for temperatures well above room temperature; the activation energy changes from 0.48 eV to 0.38 eV at higher $T$. Presumably, $Ca^{2+}$ in the grain boundaries influences the $Li^+$ arrangements in these regions. $Li^+$ order/disorder phenomena might lead to such changes.

### 3.3. Ion dynamics as seen by NMR measurements

Fig. 7a gives an overview of the $^7$Li NMR SLR rate measurements performed using an Arrhenius representation plotting the $R_{1(\rho)}$ rates as a function of the inverse temperature. To identify the thermally activated regions, we measured $R_{1(\rho)}$ of $Li_{1.4}Ca_{0.2}Zr_{1.8}(PO_4)_3$ over a wide temperature range to detect the maxima of diffusion-induced rate peaks.[48] Here we focused on the sample with the composition $Li_{1.4}Ca_{0.2}Zr_{1.8}(PO_4)_3$ as it shows the lowest bulk activation energy and the lowest amount of residual $ZrO_2$.

Below 183 K the rates $R_1$ reveal a non-diffusive background regime. In this temperature range longitudinal relaxation is induced by lattice vibrations or coupling of the Li spins with paramagnetic impurities.[48–50] At higher temperatures we expect the SLR rate to be increasingly induced by $Li^+$ hopping processes. Such processes lead to magnetic and electric field fluctuations that cause longitudinal relaxation.[48] Indeed, the rates increase with temperature and, in both cases $R_1$ and $R_{1\rho}$, characteristic diffusion-induced rate peaks appear.

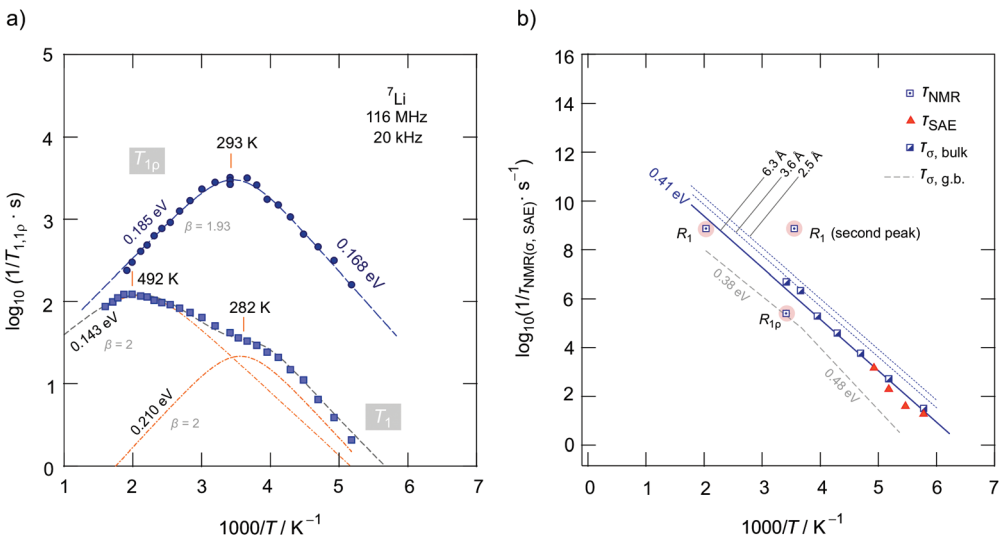


**Fig. 7** (a) Arrhenius plot of the $^7$Li NMR relaxation rates $R_1$ and $R_{1\rho}$ of $Li_{1.4}Ca_{0.2}Zr_{1.8}(PO_4)_3$ (prepared *via* the route using $ZrO_2$) measured in the laboratory frame of reference (116 MHz) and in the rotating frame of reference (20 kHz, nominal locking frequency). Dashed lines represent BPP-type fits to determine activation energies, prefactors and asymmetry parameters $\beta$. Temperatures indicate $T_{max}$ of the rate peaks. The superposition of the $R_1$ rate peaks can be approximated with two symmetric peaks ($\beta$ = 2). (b) $Li^+$ jump rates as deduced from the diffusion-induced rate peaks $R_1$ and $R_{1\rho}$. For comparison, we also included jump rates that we estimated from frequency-dependent conductivity measurements and $^7$Li SAE NMR. See text for further explanations and Table 2 for error margins of the activation energies shown.

Importantly, we recognize that $R_1$ passes through two maxima located at $T_{max}$ = 282 K and 492 K, respectively. In general, at $T_{max}$ the motional correlation rate $1/\tau_c$ is related to $\omega_0$ *via* the relation $\tau_c\omega_0 \approx 1$. The so-called motional correlation rate $1/\tau_c$ is identical, within a factor of two, with the $Li^+$ jump rate $1/\tau$.[48,50] For $R_{1\rho}$, this maximum condition changes to $\tau_c\omega_1 \approx 0.5$.[51] As $\omega_0$ and $\omega_1$ differ by more than three orders of magnitude, we are able to characterize $Li^+$ motional correlation rates in LCZP with values in both the kHz and MHz range.[52]

Here, we approximated the superposition of the two $R_1$ rate peaks by a sum of two Lorentzian-shaped spectral density functions $J(\omega_0, T) \propto \tau_c/(1 + (\omega_0\tau_c)^{\beta})$ according to the concept introduced by Bloembergen, Purcell and Pound (BPP) for 3D isotropic diffusion,[53,54] see dashed line in Fig. 7a that follows the $R_1$ rates. For each peak we used a single term to deconvolute the temperature dependence of the overall $R_1$ rates measured, *cf.* the dashed-dotted lines in Fig. 7a, which will be discussed below. The rate $1/\tau_c$ usually obeys the Arrhenius relation $1/\tau_c = 1/\tau_{c,0}\exp(-E_a/(k_BT))$; $1/\tau_{c,0}$ represents the pre-exponential factor that is typically identified as the "attempt frequency" of the jump process.[55]

In general, $J(\omega_0, T)$ is the Fourier transform of the underlying motional correlation function $G(t')$.[48] If $G(t')$ is or can be well approximated with a single exponential, $\beta$ equals 2. Values smaller than 2 are expected for correlated motion, which is, *e.g.*, seen for cations exposed to an irregularly shaped potential landscape. In such a landscape short-ranged $Li^+$ diffusion will be different to long-range ion transport. In particular, forth-and-back jumps or, more generally speaking, localized motions will govern the rate $R_1$ in the low-temperature regime, which is characterized by $\tau_c\omega_0 \gg 1$. In this regime we have $J(\omega_0) \propto {\tau_c}^{-1}{\omega_0}^{-\beta}$ with $(1 < \beta \leq 2)$. $\beta < 2$ produces asymmetric rate peaks which are often found for structurally complex ion conductors with a non-uniformly shaped energy landscape. Ion dynamics in this regime are anticipated to be affected by correlation effects because of both structural disorder and strong Coulomb interactions of the moving ions.[56] As the peak is asymmetric, the activation energy on this side of the peak, $E_{a,\,low}$, is lower than that of the high-temperature flank, $E_{a,\,high}$; the two values are linked to each other *via* $E_{a,\,low} = (\beta_{(\rho)} - 1)E_{a,\,high}$. In the regime $\tau_c\omega_0 \ll 1$, that is, on the high-temperature side of the peak, many jump events are sensed during one Larmor precession and the probability is high that also these jumps contribute to longitudinal relaxation which are characterized by higher activation energies. Usually, on this side of the rate peak $R_1(1/T)$ long-range Li ion dynamics is sensed; in this limit we obtain $J(\omega_0) \propto \tau_c$.[29]

In the present case, approximating the rate peaks with a sum of two BPP-type spectral densities yields activation energies of $E_{a,1}$ = 0.210(5) eV and $E_{a,2}$ = 0.143(5) eV. As both rate peaks join up, information on $\beta$ are difficult to obtain. Here, the fitting routine yields $\beta = 2$ for the two peaks resulting in symmetric peaks with $E_{a,\,low} = E_{a,\,high} = E_{a,i}$ $(i = 1, 2)$. Note that the peak at higher $T$ $(i = 2)$ is only partly visible which influences the precise determination of $E_{a,\,high}$. We clearly recognize that $E_{a,i}$ as determined from $R_1$ SLR NMR turned out to be significantly lower than $E_a$ obtained from $\sigma_{DC}$ measurements describing bulk ion dynamics. The fact that $E_{a,i} < E_{a,\,DC}$ shows that the number of jump events seen by NMR does not include all types of jumps needed for long-range diffusion. Obviously, the spin-fluctuations sensed by NMR are already sufficient to generate a full $R_1$ peak. Thus, we conclude that the $Li^+$ ions in LCZP are highly mobile on a short-range length scale while long-range ion transport is, however, characterized by much larger activation energies than 0.2 eV. This situation resembles that of $Li^+$ ion dynamics in argyrodite-type $Li_6PS_5I$, which has been studied recently by our group.[42] Here, we assume that rapid forward–backward exchange processes between the sites A1 and A2 might be responsible for the peaks seen in NMR spin–lattice relaxometry. A2 sites might be occupied in samples with $x > 0$. Here, especially the peak appearing at $T_{max}$ = 282 K for $Li_{1.4}Ca_{0.2}Zr_{1.8}(PO_4)_3$ points to rapid (localized) exchange processes with residence times in the order of several ns. According to $\omega_0\tau_c \approx 1$ we estimate that at $T_{max}$ the jump rate should be in the order of $1/\tau = 7.3 \times 10^8$ $s^{-1} \approx 10^9$ $s^{-1}$. A very similar behavior has recently been seen also for NaSICON-type $Na_{3.4}Sc_{0.4}Zr_{1.6}(SiO_4)_2PO_4$.

To complement our $R_1$ measurements, we carried out spin-lock NMR SLR measurements at a locking frequency of 20 kHz. As expected we detected a prominent spin-lock NMR peak $R_{1\rho}(1/T)$ at much lower temperature than 492 K. A single peak appears at $T_{max}$ = 293 K. It turned out to be slightly asymmetric with an activation energy of $E_{a,\,high}$ = 0.185(5) eV and $E_{a,\,low}$ = 0.168(5) eV. At first glance we would say that the $R_{1\rho}$ peak might correspond to the $R_1$ peak seen at $T_{max}$ = 492 K. Keeping, however, both the locking frequency of only 20 kHz and the rather low activation energy of 0.185 eV in mind, the $R_{1\rho}$ peak belonging to $R_1(1/T)$ with $T_{max}$ = 492 K would be expected to appear at much lower temperatures than ambient. Even if we replace $\omega_1$ by an effective frequency $\omega_{1,\,eff}$ $(>\omega_1)$, which takes local magnetic fields into account that increase $\omega_1$, no satisfactory joint fit results that is characterized by the same $E_a$ and the same $\tau_{c,0}$ for the two peaks. Here, only unreliably high $\omega_{1,\,eff}$ values reaching the MHz range would result in a joint fit connecting the two peaks. Table 2 shows an overview of the results obtained from analyzing the three peaks individually by BPP-type spectral density functions. It also includes the amplitudes $C_{NMR}$ in $R_{1(\rho)} = C_{NMR}J(\omega_0, T)$. We see that the amplitudes of the two $R_1$ rate peaks differ by approximately one order of magnitude. Most likely, stronger quadrupolar relaxation governs the peak appearing at higher $T$. The corresponding prefactor $1/\tau_0$ is relatively low, while that of the peak showing up at 282 K $(1/\tau_0 = 5.9 \times 10^{12}$ $s^{-1})$ is consistent with frequencies typically expected for phonons.

The above-mentioned jump rate derived from SLR NMR at $T_{max}$ $(1/\tau = 7.3 \times 10^8$ $s^{-1})$ can be converted into diffusion coefficients with the help of the Einstein–Smoluchowski equation according to $D_{NMR} = a^2/(6\tau)$, which is valid for 3D diffusion.[29] As an estimation, by inserting $a$ = 6.3 Å, which is simply the shortest Li–Li distance, we obtain $D_{NMR} = a^2/(6\tau) = 4.8 \times 10^{-11}$ $m^2$ $s^{-1}$. Assuming the interstitial sites A2 participating in exchange processes $D_{NMR}$ reduces to $1.8 \times 10^{-11}$ $m^2$ $s^{-1}$. A dis-

Table 2 Results of analyzing the $^7$Li NMR rate peaks $R_1$ and $R_{1\rho}$ of $Li_{1.4}Ca_{0.2}Zr_{1.8}(PO_4)_3$. The coupling constant $C_{NMR}$, which is the amplitude of the rate peak, $J(\omega_0) = C_{NMR}\tau_c/(1 + (\omega_0\tau_c)^\beta$, turned out to be in the range of 1010 and $10^{11}$ s$^{-2}$. Values in the order of $10^{-13}$ s for $\tau_0$ correspond to (inverse) phonon frequencies

| | $E_a$ (= $E_{a,\ high}$) | $C_{NMR}$ | $\beta_{(\rho)}$ | $\tau_0$ |
|---|---|---|---|---|
| $R_1$ ($T_{max}$ = 492 K) | 0.143(5) eV | $1.8(1) \times 10^{11}$ s$^{-2}$ | 2 | $4.1(2) \times 10^{-11}$ s |
| $R_1$ ($T_{max}$ = 282 K) | 0.210(5) eV | $2.5(1) \times 10^{10}$ s$^{-2}$ | 1.93 | $1.7(2) \times 10^{-13}$ s |
| $R_{1,\rho}$ ($T_{max}$ = 293 K) | 0.185(5) eV (0.168(5) eV)[a] | $1.5(1) \times 10^{9}$ s$^{-2}$ | 2 | $2.8(1) \times 10^{-9}$ s |

[a] The value in brackets refers to $E_{a,\ low}$ of the $R_{1\rho}$ peak seen at 293 K.



tance of $a$ = 6.3 Å is, of course, by far too long for a single hopping process. In the structural model of Catti *et al.* the distance reduced to 4.2 Å at 423 K.[24]

In the Arrhenius plot of Fig. 7b we compare the rates $1/\tau$ from NMR ($1/\tau_{NMR}$) with those obtained after converting $\sigma_{DC}$ into jump rates by using the Nernst Einstein equation. As we do not know the exact jump distance, we calculated $1/\tau_\sigma$ for three different values of $a$. $1/\tau_\sigma$ represents an average value mainly influenced by $Li^+$ jumps necessary for long-range ion transport. Most likely, the $R_1$ peak appearing at 492 K is more related to jump processes enabling the ions to move over longer distances. The large discrepancy between $1/\tau_{NMR}$(282 K) and $1/\tau_\sigma$ once again visualizes that the $R_1(1/T)$ peak at low $T$ reflects localized jump processes. We do not find evidences that this peak originates from any phase transitions, as the phase-pure Ca-bearing samples show rhombohedral structure. For comparison, in Fig. 7b we also included $1/\tau_\sigma$ rates estimated from conductivity values that characterize the influence of grain boundaries. Interestingly, $1/\tau_{NMR}$(293 K, $R_{1\rho}$) = 2.5 × $10^5$ s$^{-1}$, which we estimated *via* the relation $\omega_1\tau_c \approx 0.5$, see above, agrees with $1/\tau_{\sigma,\ g.b}$. In contrast to $R_1$, which as far as μm-sized crystallites are considered, is mainly affected by bulk processes, the corresponding spin-lock NMR rates $R_{1\rho}$ seems to be (also partly) sensitive to ion dynamics also influenced by interfacial processes. This behaviour is consistent with the following comparison. At frequencies in the kHz range ($\omega_1/2\pi$ = 20 kHz) and at $T$ = 282 K the isotherms $\sigma'(\nu)$ are mainly influenced by the g.b. response rather than bulk ion dynamics.

To shed more light on long-range ion dynamics, we used $^7$Li NMR line shape measurements and $^7$Li SAE NMR experiments[46,57–60] to further characterize ionic transport in LCZP. *Via* SAE NMR we should be able to get access to diffusion parameters that characterize ion transport over longer distances as the method is sensitive to exchange processes on the time scale that is comparable to that of DC conductivity measurements.[48] In Fig. 8a variable-temperature $^7$Li NMR spectra of $Li_{1.4}Ca_{0.2}Zr_{1.8}(PO_4)_3$ are shown. Remarkably, at temperatures as low as 213 K a relatively narrow NMR line is detected whose width is only 1.4 kHz. Usually, we would expect a width in the order of several kHz due to $^7$Li–$^7$Li dipolar interactions. Here, the large Li–Li distance of 6.3 Å between the A1 sites, and between A1 sites and Li ions occupying interstitial sites in samples with $x > 0$, leads to relatively weak dipole–dipole interactions producing a narrow line already in the rigid-lattice regime. With increasing temperature, the line undergoes a slight narrowing process because of Li diffusion that averages dipolar couplings. Finally, at even higher temperatures, *i.e.*, in the extreme narrowing regime, its width is only governed by the inhomogeneity of the external magnetic field.

Interestingly, at 313 K two satellite lines emerge that belong to a first-order quadrupole powder pattern arising from the interaction of the quadrupole moment of the $^7$Li nucleus ($I$ = 3/2) with a non-vanishing electric field gradient (EFG) at the nuclear site. The EFG is produced by the electric charge distribution in the direct neighborhood of the $^7$Li nucleus. This additional interaction alters the Zeeman levels and, thus, also the associated (angular) Zeeman frequency $\omega_0$ towards $\omega_0 \pm \omega_Q$.[32,54] The singularities seen in Fig. 8a correspond to the 90° satellite transitions of a powder pattern, which typically show up at sufficiently high $T$; this feature belongs to the universal characteristics of crystalline materials studied by NMR.[32,50,61] Their distance on the frequency scale, if we simply assume an EFG with axial symmetry, corresponds to $\delta/2$. $\delta$ is the quadrupole coupling constant. A distance of 49 kHz leads to $\delta$ = 98 kHz,[58] which is in fair agreement with the value reported by Petit *et al.*[20] Here, this value should, however, be interpreted as an average value, as we cannot exclude a small distribution of EFGs the ions are exposed to at very low temperatures. At very low $T$, the intensity of the singularities is too low to be detectable by single pulse experiments. Instead, echo experiments should be used that are able to avoid receiver dead time effects. In Fig. 8b (see inset) a spectrum is shown that is the Fourier transform of a stimulated echo. Indeed, a sharp central line is located on top of a broad quadrupole foot. Hence, we conclude that the Li ions are exposed to a distribution of EFGs.

Fluctuations in $\omega_Q$ seen by the ions when jumping between electrically inequivalent sites can be used to record sinus–sinus two-time correlation functions. In Fig. 8a the change of the $^7$Li SAE amplitude $S_2$ is shown *vs.* the logarithmic mixing time $t_m$. $S_2$ depends on both the preparation time $t_p$ and $t_m$. Here, we measured the decay curve at fixed $t_p$ (= 20 μs) but variable mixing time. Stretched exponentials of the form $S_2 \propto \exp(-(t_m/\tau_{SAE})^\lambda)$, with a stretching factor $\lambda$ ranging from 0.21 to 0.37, are best suited to describe the dependence of $S_2(t_p$ = const., $t_m)$ in this temperature regime. In general, stretching factors deviating from $\lambda$ = 1 indicate non-Debye-like motional process. For example, such deviations can arise from motions in disordered matrices or in confined dimensions[59,62] leading

 

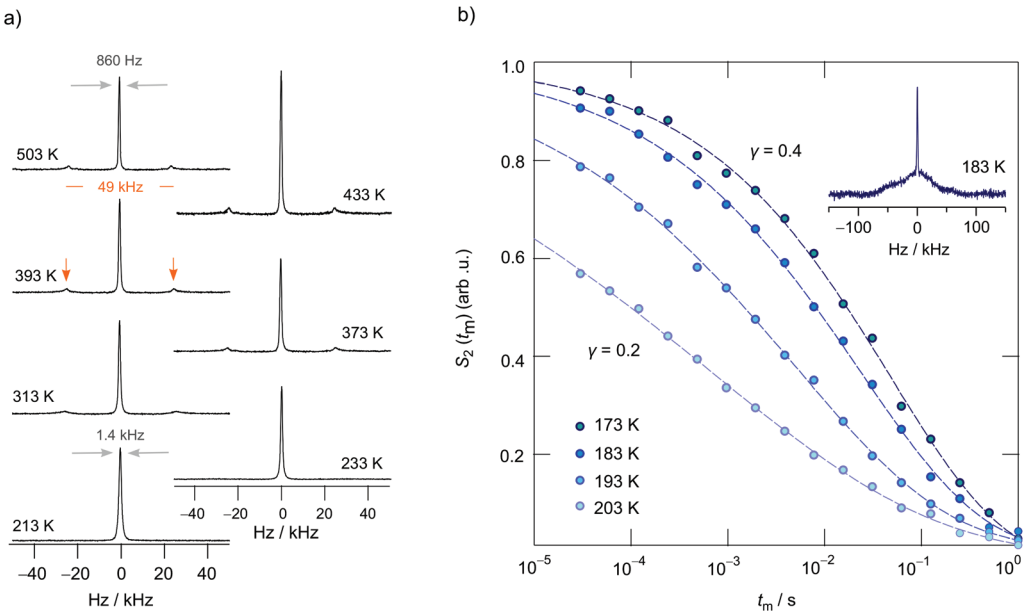


**Fig. 8** (a) $^7$Li NMR spectra of $Li_{1.4}Ca_{0.2}Zr_{1.8}(PO_4)_3$ recorded at the temperatures indicated. The NMR line transforms from a Gaussian shape at low temperatures to a Lorentzian one at elevated $T$. Clearly visible and well-defined quadrupole powder patterns emerge at temperatures higher than 313 K. (b) $^7$Li SAE NMR decay curves of LCZP whose spectra are shown in (a). Decay curves follow stretched exponentials ($0.2 < \gamma < 0.4$) which are shown as solid lines. Data have been recorded at a Larmor frequency of 116 MHz. See text for further details. Inset: Fourier transform of a spin-alignment echo, starting from the top of the echo, which was recorded at a fixed $t_p$ of 20 μs and a short mixing time of $t_m$ = 100 μs. In addition to a "central line" a rather broad quadrupole foot is visible illustrating the distribution of EFGs seen by the Li ions in the dynamic regime of the rigid lattice.

to motional correlation functions whose decay slows down with increasing observation time. With increasing $T$ the inflexion point of the echo decay curves shifts towards shorter $t_m$. At the same time, the shape of $S_2$ steadily becomes more stretched until a value of $\lambda = 0.21$ is reached at $T = 203$ K. At sufficiently long mixing times the curves $S_2(t_p = \text{const.}, t_m)$ always reach $S_{2,\infty} = 0$, which either indicates a rather large number of quadrupole frequencies involved or which points to the influence of dipolarly coupled spins, as is well-described in literature.[36] The rates $1/\tau_{SAE}$ governing the stretched decay functions are included in Fig. 7b. We recognize that they are in fair agreement with those rates, $1/\tau_{\sigma,\ bulk}$, which were estimated from bulk ionic conductivities of $Li_{1.4}Ca_{0.2}Zr_{1.8}(PO_4)_3$.

## 4. Conclusion

We used a conventional solid-state reaction procedure to synthesize NaSICON-type $LiZr_2(PO_4)_3$ and investigated both its ionic conductivity and $Li^+$ diffusivity by broadband conductivity measurements and NMR spectroscopy. $Ca^{2+}$ incorporation helps prepare $Li_{1+2x}Zr_{2-x}Ca_x(PO_4)_3$ crystallizing with rhombohedral symmetry. While bulk ion dynamics is not influenced by the $Ca^{2+}$ content, the grain boundaries in LZCP turn out to be less blocking for $Li^+$ ions as compared to the sample with $x = 0$. We observed an increase in the low-frequency ionic conductivity by two orders of magnitude when increasing $x$ from $x = 0$ to $x = 0.2$. For $Li_{1.4}Ca_{0.2}Zr_{1.8}(PO_4)_3$ $^7$Li NMR relaxometry revealed rapid localized $Li^+$ jump processes with activation energies of 0.21 eV and 0.14 eV. The diffusion-induced rate peak seen at 282 K points to a very high jump rate in the order of $10^9$ $s^{-1}$ at this temperature. On the other hand, $^7$Li spin-alignment echo spectroscopy confirmed that long-range ion transport in the bulk regions of $Li_{1.4}Zr_{1.8}Ca_{0.2}(PO_4)_3$ needs to be characterized by an activation energy of 0.41 eV as determined by variable-frequency conductivity measurements.

## Conflicts of interest

There are no conflicts to declare.

## Acknowledgements

This project has received funding from the European Union's Horizon 2020 research and innovation programme under grant agreement no. 769929. We thank the Deutsche Forschungsgemeinschaft for further support (FOR1277, WI3600(2-1;4-2). Further support by the K-project 'safe battery' (FFG) is highly appreciated.

## References

1 J. Janek and W. G. Zeier, *Nat. Energy*, 2016, **1**, 16141.
2 D. Larcher and J. M. Tarascon, *Nat. Chem.*, 2015, **7**, 19–29.

3 J. I. Hur, L. C. Smith and B. Dunn, *Joule*, 2018, **2**, 1187–1201.
4 E. Quartarone and P. Mustarelli, *Chem. Soc. Rev.*, 2011, **40**, 2525–2540.
5 J. C. Bachman, S. Muy, A. Grimaud, H. H. Chang, N. Pour, S. F. Lux, O. Paschos, F. Maglia, S. Lupart, P. Lamp, L. Giordano and Y. Shao-Horn, *Chem. Rev.*, 2016, **116**, 140–162.
6 Z. Z. Zhang, Y. J. Shao, B. Lotsch, Y. S. Hu, H. Li, J. Janek, L. F. Nazar, C. W. Nan, J. Maier, M. Armand and L. Q. Chen, *Energy Environ. Sci.*, 2018, **11**, 1945–1976.
7 Y. Inaguma, K. Funayama, A. Aimi, D. Mori, Y. Hamasaki, K. Ueda, M. Ikeda, T. Ohno and K. Mitsuishi, *Solid State Ionics*, 2018, **321**, 29–33.
8 A. Sakuda, A. Hayashi and M. Tatsumisago, *Sci. Rep.*, 2013, **3**, 2261.
9 A. Hayashi, K. Noi, A. Sakuda and M. Tatsumisago, *Nat. Commun.*, 2012, **3**, 856.
10 M. Guin and F. Tietz, *J. Power Sources*, 2015, **273**, 1056–1064.
11 M. Guin, F. Tietz and O. Guillon, *Solid State Ionics*, 2016, **293**, 18–26.
12 H. Xie, J. B. Goodenough and Y. Li, *J. Power Sources*, 2011, **196**, 7760–7762.
13 V. Ramar, S. Kumar, S. R. Sivakkumar and P. Balaya, *Electrochim. Acta*, 2018, **271**, 120–126.
14 S. Hasegawa, N. Imanishi, T. Zhang, J. Xie, A. Hirano, Y. Takeda and O. Yamamoto, *J. Power Sources*, 2009, **189**, 371–377.
15 Y. T. Li, W. D. Zhou, X. Chen, X. J. Lu, Z. M. Cui, S. Xin, L. G. Xue, Q. X. Jia and J. B. Goodenough, *Proc. Natl. Acad. Sci. U. S. A.*, 2016, **113**, 13313–13317.
16 H. Xie, Y. Li and J. B. Goodenough, *RSC Adv.*, 2011, **1**, 1728–1731.
17 C. R. Mariappan, P. Kumar, A. Kumar, S. Indris, H. Ehrenberg, G. Vijaya Prakash and R. Jose, *Ceram. Int.*, 2018, **44**, 15509–15516.
18 L. Xiaojuan, F. Xue, L. Wenwei, L. Haitao and Z. Yunjie, Adv. Engin. Res., International Conference on Advances in Energy, Environment and Chemical Engineering, 2015, pp. 227–230, DOI: DOI: 10.2991/aeece-15.2015.45.
19 D. Petit, P. Colomban, G. Collin and J. P. Boilot, *Mater. Res. Bull.*, 1986, **21**, 365–371.
20 D. Petit and B. Sapoval, *Solid State Ionics*, 1986, **21**, 293–304.
21 M. Casciola, U. Costantino, L. Merlini, I. G. K. Andersen and E. K. Andersen, *Solid State Ionics*, 1988, **26**, 229–235.
22 M. Catti and S. Stramare, *Solid State Ionics*, 2000, **136–137**, 489–494.
23 M. Catti, S. Stramare and R. Ibberson, *Solid State Ionics*, 1999, **123**, 173–180.
24 M. Catti, A. Comotti and S. Di Blas, *Chem. Mater.*, 2003, **15**, 1628–1632.
25 H. El-Shinawi, C. Greaves and J. Janek, *RSC Adv.*, 2015, **5**, 17054–17059.
26 F. Preishuber-Pflügl, P. Bottke, V. Pregartner, B. Bitschnau and M. Wilkening, *Phys. Chem. Chem. Phys.*, 2014, **16**, 9580–9590.
27 S. Lunghammer, Q. Ma, D. Rettenwander, I. Hanzu, F. Tietz and H. M. R. Wilkening, *Chem. Phys. Lett.*, 2018, **701**, 147–150.
28 B. Stanje, D. Rettenwander, S. Breuer, M. Uitz, S. Berendts, M. Lerch, R. Uecker, G. Redhammer, I. Hanzu and M. Wilkening, *Ann. Phys.*, 2017, **529**, 1700140.
29 M. Uitz, V. Epp, P. Bottke and M. Wilkening, *J. Electroceram.*, 2017, **38**, 142–156.
30 V. Epp, Q. L. Ma, E. M. Hammer, F. Tietz and M. Wilkening, *Phys. Chem. Chem. Phys.*, 2015, **17**, 32115–32121.
31 N. P. Kuz'mina, A. E. Altsybeev, I. P. Malkerova, A. S. Alikhanyan and I. E. Korsakov, *Russ. J. Inorg. Chem.*, 2006, **51**, 1750–1754.
32 V. Epp, Ö. Gün, H. J. Deiseroth and M. Wilkening, *Phys. Chem. Chem. Phys.*, 2013, **15**, 7123.
33 E. Fukushima and S. B. W. Roeder, *Experimental Pulse NMR. A Nuts and Bolts Approach*, Addison-Wesley Publ. Comp., Reading, 1981.
34 R. Böhmer, *J. Magn. Reson.*, 2000, **147**, 78–88.
35 J. Jeener and P. Broekaert, *Phys. Rev.*, 1967, **157**, 232–240.
36 F. Qi, G. Diezemann, H. Böhm, J. Lambert and R. Böhmer, *J. Magn. Reson.*, 2004, **169**, 225–239.
37 C. Masquelier, C. Wurm, J. Rodríguez-Carvajal, J. Gaubicher and L. Nazar, *Chem. Mater.*, 2000, **12**, 525–532.
38 A. Aatiq, M. Ménétrier, L. Croguennec, E. Suard and C. Delmas, *J. Mater. Chem.*, 2002, **12**, 2971–2978.
39 K. Arbi, M. Ayadi-Trabelsi and J. Sanz, *J. Mater. Chem.*, 2002, **12**, 2985–2990.
40 I. A. Stenina, Y. A. Velikodnyi, V. A. Ketsko and A. B. Yaroslavtsev, *Inorg. Mater.*, 2004, **40**, 967–970.
41 J. Sanz, J. M. Rojo, R. Jiménez, J. E. Iglesias and J. Alamo, *Solid State Ionics*, 1993, **62**, 287–292.
42 I. Hanghofer, M. Brinek, S. L. Eisbacher, B. Bitschnau, M. Volck, V. Hennige, I. Hanzu, D. Rettenwander and H. M. R. Wilkening, *Phys. Chem. Chem. Phys.*, 2019, **21**, 8489–8507.
43 A. K. Jonscher, *Nature*, 1977, **267**, 673–679.
44 D. L. Sidebottom, *Phys. Rev. Lett.*, 1999, **83**, 983–986.
45 J. T. S. Irvine, D. C. Sinclair and A. R. West, *Adv. Mater.*, 1990, **2**, 132–138.
46 B. Ruprecht, H. Billetter, U. Ruschewitz and M. Wilkening, *J. Phys.: Condens. Matter*, 2010, **22**, 245901.
47 S. Breuer, D. Prutsch, Q. L. Ma, V. Epp, F. Preishuber-Pflügl, F. Tietz and M. Wilkening, *J. Mater. Chem. A*, 2015, **3**, 21343–21350.
48 M. Wilkening and P. Heitjans, *ChemPhysChem*, 2012, **13**, 53–65.
49 M. Wilkening, V. Epp, A. Feldhoff and P. Heitjans, *J. Phys. Chem. C*, 2008, **112**, 9291–9300.
50 A. Kuhn, S. Narayanan, L. Spencer, G. Goward, V. Thangadurai and M. Wilkening, *Phys. Rev. B: Condens. Matter Mater. Phys.*, 2011, **83**, 094302.

51 A. Kuhn, M. Kunze, P. Sreeraj, H. D. Wiemhöfer, V. Thangadurai, M. Wilkening and P. Heitjans, *Solid State Nucl. Magn. Reson.*, 2012, **42**, 2–8.
52 M. Wilkening, V. Epp, A. Feldhoff and P. Heitjans, *J. Phys. Chem. C*, 2008, **112**, 9291–9300.
53 N. Bloembergen, E. M. Purcell and R. V. Pound, *Phys. Rev.*, 1948, **73**, 679–712.
54 A. Abragam, *The Principles of Nuclear Magnetism*, Claredon Press, Oxford, 1961.
55 P. M. Richards, in *Topics in Current Physics*, ed. M. B. Salamon, Springer, Berlin, 1979, vol. 15.
56 A. Bunde, P. Maass and M. Meyer, *Phys. A*, 1992, **191**, 433–437.
57 P. Bottke, D. Rettenwander, W. Schmidt, G. Amthauer and M. Wilkening, *Chem. Mater.*, 2015, **27**, 6571–6582.
58 M. Wilkening and P. Heitjans, *J. Phys.: Condens. Matter*, 2006, **18**, 9849–9862.
59 M. Wilkening and P. Heitjans, *Phys. Rev. B: Condens. Matter Mater. Phys.*, 2008, **77**, 024311.
60 M. Wilkening, A. Kuhn and P. Heitjans, *Phys. Rev. B*, 2008, **78**, 054303.
61 R. Bertermann, W. Müller-Warmuth, C. Jansen, F. Hiltmann and B. Krebs, *Solid State Ionics*, 1999, **117**, 245–255.
62 P. Bottke, Y. Ren, I. Hanzu, P. G. Bruce and M. Wilkening, *Phys. Chem. Chem. Phys.*, 2014, **16**, 1894–1901.